AEROSOL EFFECTS ON SIMULATED SUPERCELL THUNDERSTORMS

IN ENVIRONMENTS WITH DIFFERENT RELATIVE HUMIDITY AND VERTICAL WIND SHEAR

Evan A. Kalina* and Katja Friedrich

Department of Atmospheric and Oceanic Sciences, University of Colorado, Boulder, Colorado

Hugh Morrison and George H. Bryan

National Center for Atmospheric Research, Boulder, Colorado

1. INTRODUCTION

A variety of convective modes and processes have been shown to exhibit sensitivity to aerosol concentration (e.g., Khain et al. 2005; van den Heever and Cotton 2007; Khain and Lynn 2009; Mansell and Ziegler 2013). However, there is a lack of research that examines how the microphysical processes and resulting thermodynamic structure of thunderstorms vary across the wide range of aerosol concentrations that are possible within the atmosphere. Specifically, it is unclear at what aerosol concentration perturbed microphysical processes become evident, and whether these perturbations continue to grow as aerosol concentration increases or if additional increases have negligible influence above a certain threshold. Further, how these trends are affected by changes in the low-level relative humidity and vertical wind shear of the environment is uncertain.

In unpolluted conditions over the open ocean, aerosol number concentrations may be as small as 100 cm^{-3}, while environments contaminated by smoke from forest fires may feature concentrations in excess of 10 000 cm^{-3} (Andreae et al. 2004). Data from the Southern Great Plains (SGP) site of the Atmospheric Radiation Measurement (ARM) Climate Research Facility in Lamont, Oklahoma demonstrate that near-surface cloud condensation nuclei (CCN) concentrations on the U.S. Great Plains frequently vary between 1000 cm^{-3} and 5000 cm^{-3} on supercell thunderstorm days, and can even approach 10 000 cm^{-3} on days with ordinary convection. Such widely varying CCN number concentration may play an important role in modifying precipitation development in the supercell thunderstorms that commonly affect the Great Plains, since the growth of precipitating liquid hydrometeors starts when water vapor condenses onto CCN to form cloud droplets. The cloud droplet activation rate is affected by the

type and size of the aerosols that serve as CCN, and competition for a limited amount of water makes the aerosol concentration critical in determining how large cloud droplets can grow and, therefore, how efficient autoconversion into raindrops will be. Because aerosols can change the rates of cloud microphysical processes, they can also alter the local temperature and moisture profiles by modifying the latent cooling/heating that results from phase changes of water. In this manner, the buoyancy, precipitation efficiency, and the lifetime of the cloud can all be affected by changes in the aerosol properties. For more information about cloud-aerosol interactions, the reader is directed to Levin and Cotton (2009) and Tao et al. (2012).

To understand the response of supercell thunderstorms to a variety of aerosol concentrations, the Weather Research and Forecasting (WRF) model is run at a cloud-resolving horizontal resolution (1 km) with the Morrison microphysics scheme, in which the concentration of cloud condensation nuclei (CCN) at 1% supersaturation is varied from 100 cm^{-3} to 10 000 cm^{-3}. Four different environmental soundings are tested (Table 1 and Fig. 1), all of which are supportive of supercell thunderstorms (i.e., thunderstorms with rotating updrafts), which may produce large hail, damaging straight-line winds, flooding, and tornadoes. Vertically-integrated mass budgets are analyzed to quantify the effect of increasing CCN concentration on rates of riming, melting, droplet collection, and evaporation. In addition, these perturbed microphysical processes are linked to changes in the low-level cold pool and to differences in accumulated surface precipitation to understand how supercell thunderstorms respond across the wide spectrum of plausible atmospheric aerosol concentrations.

_____

* Corresponding author address: Evan A. Kalina, Department of Atmospheric and Oceanic Sciences, University of Colorado, 311 UCB, Boulder, CO, 80309. Email: evan.kalina@colorado.edu

TABLE 1. Relative humidity (RH) and Convective Available Potential Energy (CAPE) for the soundings used to initialize the WRF model in the default (def), low relative humidity (loRH), high relative humidity (hiRH), and high vertical wind shear (hiWS) cases.

Case	Mean RH (sfc-800 mb)	Surface CAPE
def	79.9	2745
loRH	61.3	967
hiRH	90.9	5138
hiWS	79.9	2745

2. MODEL CONFIGURATION

This study uses version 3.3 of the three-dimensional, non-hydrostatic Weather Research and Forecasting (WRF) model (Skamarock et al. 2008) with the Advanced Research WRF (ARW) core. The chosen model configuration is similar to the idealized supercell thunderstorm test case that is provided with WRF and to those of Morrison and Milbrandt (2011), Lebo et al. (2012), and Morrison (2012). Idealized simulations are chosen so that the effect of CCN concentration on the microphysics and thermodynamics of the supercell thunderstorm can be quantified in the absence of secondary feedbacks from radiative, boundary layer, and surface layer processes. The domain has a horizontal grid spacing of 1 km and spans 200 km in both the zonal and meridional directions. The horizontal boundaries are periodic to ensure conservation of total mass within the domain. A time step of 2 s is used, except for the acoustic modes, for which a 0.33-s time step is used. In the vertical, an exponentially stretched grid with 70 levels and a nearly constant spacing of ~300 m is selected. The model top is at z = 24 km, and a Rayleigh damper with a damping coefficient of 0.003 s^{-1} is used within the upper 5 km to eliminate gravity waves that reflect off the upper boundary.

Horizontal and vertical advection are calculated using fifth- and third-order monotonic schemes, respectively. Turbulent diffusion is computed with a 1.5-order turbulent kinetic energy scheme (Skamarock et al. 2008). Radiative transfer, surface fluxes, and Coriolis force are neglected for simplicity. Convection is initiated with a warm perturbation in the potential temperature field. The maximum amplitude of the perturbation is 3 K, it is centered at z = 1.5 km, and it is 20 km wide in the horizontal and 3 km in height. The model equations are integrated for two hours, with output written every 10 minutes.

The Morrison double-moment microphysics scheme (Morrison and Pinto 2005; Morrison et al. 2005; Morrison et al. 2009) is selected to model microphysical processes. The scheme considers five hydrometeor species, all of which are assumed to consist of spherical particles: cloud droplets, cloud ice, rain, snow, and a rimed ice category with bulk density and fall speed characteristics that are typical of either graupel or hail (user selectable). In this research, hail is chosen as the rimed ice category, which may be more suitable than graupel for studies of continental deep convection (McCumber et al. 1991; Bryan and Morrison 2012). The hydrometeor size distributions $N(D)$ are represented by gamma functions of the form

$$N(D) = N_0 D^\mu e^{-\lambda D}, \tag{1}$$

where D is the particle diameter, N_0 is the intercept parameter, μ is the shape parameter, and λ is the slope parameter. N_0 and λ are predicted for each hydrometeor species via Eqs. (2) and (3).

$$N_0 = \frac{N\lambda^{\mu+1}}{\Gamma(\mu+1)} \tag{2}$$

$$\lambda = \left[\frac{cN\Gamma(\mu+4)}{q\Gamma(\mu+1)} \right]^{\frac{1}{3}} \tag{3}$$

where q is the hydrometeor mass mixing ratio, Γ is the Euler gamma function and $c = \pi/6 \times \rho$, where ρ is the bulk density of the hydrometeor class, given by Table 4 in Morrison and Milbrandt (2011).

For cloud ice, snow, and hail, μ is set to zero. For cloud droplets, the value of μ is a function of the predicted cloud droplet number concentration according to Martin et al. (1994) and varies from 2 to 10. In this research, a variable shape parameter for the raindrop size distribution is used. Specifically, μ is diagnosed with the shape-slope relation from Cao et al. (2008), allowing μ to vary with λ (Eq. 4).

$$\mu = -0.0201\lambda^2 + 0.902\lambda - 1.718 \tag{4}$$

The use of a variable μ scheme for rain helps address the problem of excessive size sorting that has been noted in double-moment bulk microphysics schemes with fixed μ, and more closely approximates the narrowing of the drop size distribution and the increase in raindrop mean-mass diameter that have been observed due to size sorting (Wacker and Seifert 2001; Milbrandt and Yau 2005; Milbrandt and McTaggart-Cowan 2010; Kumjian and Ryzhkov 2012). To determine μ within the microphysics scheme, an initial guess of μ = 0 is made and Eqs. (3) and (4) are iterated until λ converges to within 0.1%. This formula is not extrapolated to values of λ larger than the Cao et al. (2008) data range (20 mm^{-1}), giving a maximum μ of approximately 8.28. The minimum allowed μ for rain is 0. In section 3d, results from the variable μ scheme are compared to results from a set of μ = 0 simulations with the default sounding.

Here, the CCN spectrum is represented by a power law relationship (Eq. 5; Pruppacher and Klett 1997).

$$N_{CCN} = CS^k \qquad\qquad\qquad (5)$$

In Eq. (5), N_{CCN} is the number concentration of activated cloud condensation nuclei (cm^{-3}), S is the supersaturation ratio in percent, C is the CCN concentration (cm^{-3}) at S = 1%, and k is a unitless constant. As S increases, more CCN activate. Tables 9.1 and 9.2 in Pruppacher and Klett (1997) demonstrate that while C is observed to be larger in continental vs. maritime air masses, there is no clear dependence of k on the type of air mass or on the value of C. Therefore, in this study, we assume that k is equal to 0.7, which is the average of the values in Pruppacher and Klett (1997). For simplicity, the initial vertical distribution of CCN is assumed to be constant with height and CCN transport is not considered. The total number concentration of CCN plus cloud droplets within a grid cell remains constant throughout the simulation. As cloud droplets are converted into raindrops and ice crystals, new CCN are added to the grid cell to replace the cloud droplets. Simulations are conducted for 15 different values of C that range between 100 cm^{-3} and 10 000 cm^{-3}: 100, 250, 500, 750, 1000, 1500, 2000, 3000, 4000, 5000, 6000, 7000, 8000, 9000, and 10 000 cm^{-3}.

3. RESULTS

3.1 Microphysical Effects

We begin by examining the differences in the diameter (Fig. 2) and number concentration (Fig. 3) of cloud droplets, rain, and hail particles for the cleanest (CCN = 100 cm^{-3}) and dirtiest (CCN = 10 000 cm^{-3}) runs of each of the four soundings. These figures consist of conditional (i.e., only non-zero values), domain-averaged vertical profiles at t = 120 min. Due to more CCN, the dirtiest simulation (independent of the initial sounding) has smaller (5 μm vs. 17 μm; Fig. 2), more numerous (~4000 cm^{-3} vs. ~100 cm^{-3}; Fig. 3) cloud droplets than the cleanest simulation. Because the mean cloud droplet size is smaller in the dirtiest run, fewer cloud droplets make the transition into rain and hail particles, with a 97% (85%) smaller number concentration of rain (hail) at 5 km (10 km) compared to the cleanest simulation of the def sounding (Fig. 3a; note that a logarithmic scale is used). Similar trends are reflected in the number concentration profiles that result from the other soundings (Fig. 3b-3d). Although there are fewer raindrops and hailstones in the dirtiest simulation, the rain and hail particles that are present have three times the cloud water mass available for collection (0.9 g kg^{-1} vs. 0.3 g kg^{-1} at 9 km; not shown), which leads to mean mass diameters that are 30% larger for rain and 3% larger for hail near the surface in the dirtiest run with the def sounding (Fig. 2a). For the other soundings, the only notable departure from this pattern is with the loRH sounding, in which the mean mass diameter of rain is about equal in the cleanest and dirtiest runs near the surface (Fig. 2c), despite being larger in the dirtiest run from 2-8 km (as in the other soundings).

To understand the differences in mean diameter and number concentration between the cleanest and dirtiest runs, we now examine how the individual microphysical process rates vary across all of the CCN concentrations (Fig. 4). From this figure, it is apparent that it is not necessary for the CCN concentration to be increased to 10 000 cm^{-3} for the microphysical processes to be perturbed. In fact, for each of the soundings, perturbations in the rates of vertically-integrated melting, evaporation, and riming of hailstones generally saturate by CCN = 3000 cm^{-3}, after which these rates exhibit little change. The microphysical processes that directly involve cloud droplets (i.e., collection of cloud droplets by rain and riming of hailstones by cloud droplets) are most sensitive to further increases in CCN concentration above 2000-3000 cm^{-3}, although the rate of change in these processes is generally smaller above CCN = 3000 cm^{-3} in each of the soundings. These results suggest that extreme concentrations of CCN, such as those observed downwind of forest fires or highly polluted urban areas, may not be necessary to perturb the microphysical processes substantially. Further, after the CCN concentration exceeds 3000 cm^{-3}, additional increases in CCN concentration have progressively less impact on the microphysical processes in the model configuration used here.

3.2 Cold Pool Effects

Figure 5 depicts the variation in the size and the mean perturbation potential temperature (θ') of the cold pool ($\theta' <$ -2K at z = 170 m) with CCN concentration. It is evident from this figure that the relationship between the cold pool characteristics and the CCN concentration is not monotonic, in contrast to what has been reported or suggested in several other studies of supercell thunderstorms (e.g., Lerach et al. 2008; Storer et al. 2010; Lerach and Cotton 2012). In addition, the response of the cold pool to CCN concentration is highly dependent on the initial sounding used: In def (Fig. 5a) and hiRH (Fig. 5b), the cold pool size at t = 120 min remains nearly constant at 6400 km^2 regardless of the CCN concentration, while the mean cold pool temperature increases by ~0.4 K from CCN = 100 cm^{-3} to CCN = 4000 cm^{-3} before remaining nearly constant at larger CCN concentrations. In contrast, loRH (Fig. 5c) exhibits a rapid decrease in cold pool size at t = 120 min, from 1200 km^2 (CCN = 100 cm^{-3}) to 400 km^2 (CCN = 3000 cm^{-3}), followed by a much more gradual decrease from 400 km^2 to 250 km^2 between CCN = 3000 cm^{-3} and CCN = 10 000 cm^{-3}. The response of the cold pool in hiWS (Fig. 5d) is similar to that of loRH, with a rapid decrease in cold pool size from 7700 km^2 (CCN = 100 cm^{-3}) to 6000 km^2 (CCN = 3000 cm^{-3}), followed by nearly constant size between CCN = 3000 cm^{-3} and CCN = 10 000 cm^{-3}. The cold pools of loRH and hiWS are more responsive to changes in CCN concentration due to the decreased rate of melting as CCN concentration increases in these cases (Fig. 4c-d). In contrast, little change in the amount of melting

occurs as the CCN concentration is increased in def and hiRH (Fig. 4a-b), leading to a smaller change in the evaporative cooling rate relative to loRH and hiWS.

3.3 Precipitation Effects

Similar to that of the cold pool characteristics, the response of the domain-averaged precipitation to increases in CCN concentration (Fig. 6) is dependent on environmental conditions. For def (Fig. 6a), the domain-averaged precipitation increases by ~0.1 mm as the CCN concentration is increased from CCN = 100 cm^{-3} to CCN = 1000 cm^{-3}, rises much more slowly from CCN = 1000 cm^{-3} to its peak at CCN = 5000 cm^{-3}, and then slowly declines by ~0.03 mm between CCN = 5000 cm^{-3} and CCN = 10 000 cm^{-3}. The pattern for hiRH (Fig. 6b) is similar, but the initial increase in precipitation between CCN = 100 cm^{-3} and CCN = 1000 cm^{-3} is larger than in def (0.2 mm versus 0.1 mm), and for each of the time steps, the precipitation reaches a peak value between CCN = 2000 cm^{-3} and CCN = 4000 cm^{-3} and then remains roughly constant through CCN = 10 000 cm^{-3}, rather than slowly decreasing as in def. In contrast, increasing CCN concentration causes domain-averaged precipitation to decline nearly monotonically in loRH (Fig. 6c), with the most rapid decrease in precipitation from CCN = 100 cm^{-3} to CCN = 3000 cm^{-3}. In addition, while the absolute change in domain-averaged precipitation in loRH is similar to that of the other soundings (~0.1 mm at t = 120 min), the relative change is much larger in loRH (50% vs. ~10%) due to the small total precipitation (~0.16 mm vs. 1.3-2.0 mm). Overall, our results show that the largest changes in precipitation for each of the four soundings are achieved between CCN = 100 cm^{-3} and CCN = 3000 cm^{-3} (Fig. 6), with much smaller changes at CCN concentrations larger than 3000 cm^{-3}. This pattern mirrors that of the vertically-integrated microphysical process rates shown in Fig. 4, which also change much more gradually once the CCN concentration exceeds 3000 cm^{-3}.

The spatial distribution of the accumulated precipitation (Fig. 7) reveals a few important differences between the cleanest and dirtiest runs for each sounding. First, the most polluted runs of def (Fig. 7a) and hiRH (Fig. 7b) have up to 25 mm more precipitation along (and to the immediate left) of the tracks of both the left- and right-moving updrafts. This trend is also partly reflected in hiWS, although the enhancement in precipitation along the updraft tracks in the most polluted run is up to 18 mm and is less spatially uniform than in def and hiRH. The pattern is completely different in loRH, however, with *decreases* in accumulated precipitation of up to 18 mm along and to the right of the updraft tracks in the most polluted case. In def, hiRH, and hiWS, the left-moving updraft moves farther to the left in the most polluted run, especially after t = 60 min in hiRH and t = 80 min in def and hiWS. This shift in the track of the left-

moving updraft is therefore at least partly responsible for the precipitation enhancement along and to the left of the left-moving updraft in the dirtiest runs of def, hiRH, and hiWS, and demonstrates that the CCN concentration can indirectly influence the path of the supercell thunderstorm, likely by changing the characteristics of the low-level cold pool. However, the enhanced precipitation along and to the left of the right-moving updraft cannot be attributed to a track shift, as the path of the right-moving updraft either remains the same (hiWS) or shifts slightly to the right (def/hiRH) in the most polluted runs.

4. CONCLUSIONS

The results herein highlight the complex interactions between microphysical processes, precipitation, and thermodynamics in supercell thunderstorms and the sensitivity that these processes display towards pollutant concentration and environmental conditions. While changes in the individual microphysical process rates may be fairly large and monotonic, the impacts on the cold pool characteristics and the accumulated precipitation are generally smaller (in a relative sense) and non-monotonic due to compensating changes in the microphysical processes. Low-precipitation supercell thunderstorms, however, may be an exception to this statement. Here, an 84% reduction in the cold pool area and a 50% decrease in the domain-averaged precipitation occurred in polluted conditions with dry low-level relative humidity. This result indicates that the response of supercell thunderstorms to CCN concentration is highly dependent on the environmental conditions, even in an idealized modeling framework in which the secondary feedback between the initial conditions and physical processes such as radiative transfer and surface fluxes are neglected. Since differences in the relative humidity and vertical wind shear can change the cold pool and precipitation responses to CCN concentration, future studies that examine observational evidence to validate the trends seen in numerical models will likely need to stratify results by environmental conditions.

5. ACKNOWLEDGMENTS

6. REFERENCES

Andreae, M. O., D. Rosenfeld, P. Artaxo, A. A. Costa, G. P. Frank, K. M. Longlo, and M. A. F. Silva-Dias, 2004: Smoking rain clouds over the Amazon. *Science*, **303**, 1337–1342.

Brown, D., R. Brownrigg, M. Haley, and W. Huang, 2012: The NCAR Command Language (NCL) (version 6.0.0). UCAR/NCAR Computational and Information Systems Laboratory, Boulder, CO. [Available online at http://dx.doi.org/10.5065/D6WD3XH5.]

Bryan, G. H., and H. Morrison, 2012: Sensitivity of a simulated squall line to horizontal resolution and parameterization of microphysics. *Mon. Wea. Rev.*, **140**, 202–225.

Cao, Q., G. Zhang, E. Brandes, T. Schuur, A. Ryzhkov, and K. Ikeda, 2008: Analysis of video disdrometer and polarimetric radar data to characterize rain microphysics in Oklahoma. *J. Appl. Meteor. Climatol.*, **47**, 2238–2255.

Khain, A. P., and B. Lynn, 2009: Simulation of a supercell storm in clean and dirty atmosphere using weather research and forecast model with spectral bin microphysics. *J. Geophys. Res.*, **114**, D19209.

Khain, A. P., D. Rosenfeld, and A. Pokrovsky, 2005: Aerosol impact on the dynamics and microphysics of deep convective clouds. *Quart. J. Roy. Meteor. Soc.*, **131**, 2639–2663.

Kumjian, M. R., and A. V. Ryzhkov, 2012: The impact of size sorting on the polarimetric radar variables. *J. Atmos. Sci.*, **69**, 2042–2060.

Lebo, Z. J., H. Morrison, and J. H. Seinfeld, 2012: Are simulated aerosol-induced effects on deep convective clouds strongly dependent on saturation adjustment? *Atmos. Chem. Phys.*, **12**, 9941–9964.

Lerach, D. G., and W. R. Cotton, 2012: Comparing aerosol and low-level moisture influences on supercell tornadogenesis: Three-dimensional idealized simulations. *J. Atmos. Sci.*, **69**, 969–987.

Lerach, D. G., B. J. Gaudet, and W. R. Cotton, 2008: Idealized simulations of aerosol influences on tornadogenesis. *Geophys. Res. Lett.*, **35**, L23806. doi:10.1029/2008GL035617.

Levin, Z., and W. R. Cotton, Eds., 2009: *Aerosol Pollution Impact on Precipitation: A Scientific Review*. Springer, 386 pp.

Mansell, E. R., and C. L. Ziegler, 2013: Aerosol effects on simulated storm electrification and precipitation in a two-moment bulk microphysics model. *J. Atmos. Sci.*, **70**, 2032–2050.

Martin, G. M., D. W. Johnson, and A. Spice, 1994: The measurement and parameterization of effective radius of droplets in warm stratocumulus clouds. *J. Atmos. Sci.*, **51**, 1823–1842.

McCumber, M., W. K. Tao, J. Simpson, R. Penc, and S. T. Soong, 1991: Comparison of ice-phase microphysical parameterization schemes using numerical simulations of tropical convection. *J. Appl. Meteor.*, **30**, 985–1004.

Milbrandt, J. A., and M. K. Yau, 2005: A multimoment bulk microphysics parameterization. Part I: Analysis of the role of the spectral shape parameter. *J. Atmos. Sci.*, **62**, 3051–3064.

Milbrandt, J. A., and R. McTaggart-Cowan, 2010: Sedimentation-induced errors in bulk microphysics schemes. *J. Atmos. Sci.*, **67**, 3931–3948.

Morrison, H., 2012: On the robustness of aerosol effects on an idealized supercell storm simulated with a cloud system-resolving model. *Atmos. Chem. Phys.*, **12**, 7689–7705.

Morrison, H., and J. O. Pinto, 2005: Mesoscale modeling of springtime arctic mixed-phase stratiform clouds using a new two-moment bulk microphysics scheme. *J. Atmos. Sci.*, **62**, 3683–3704.

Morrison, H., and J. A. Milbrandt, 2011: Comparison of two-moment bulk microphysics schemes in idealized supercell thunderstorm simulations. *Mon. Wea. Rev.*, **139**, 1103–1130.

Morrison, H., J. A. Curry, and V. I. Khvorostyanov, 2005: A new double-moment microphysics parameterization for application in cloud and climate models. Part I: Description. *J. Atmos. Sci.*, **62**, 1665–1677.

Morrison, H., G. Thompson, and V. Tatarskii, 2009: Impact of cloud microphysics on the development of trailing stratiform precipitation in a simulated squall line: Comparison of one- and two-moment schemes. *Mon. Wea. Rev.*, **137**, 991–1007.

Pruppacher, H. R., and J. D. Klett, 1997: *Microphysics of Clouds and Precipitation.* 2nd ed. Kluwer Academic, 954 pp.

Skamarock, W. C., and Coauthors, 2008: A description of the advanced research WRF version 3. NCAR Tech. Note NCAR/TN-475+STR, 113 pp.

[Available online at http://www.mmm.ucar.edu/wrf/users/docs/arw_v3.pdf.]

Storer, R. L., S. van den Heever, and G. L. Stephens, 2010: Modeling aerosol impacts on convective storms in different environments. *J. Atmos. Sci.*, **67**, 3904–3915.

Tao, W.-K., J.-P. Chen, Z. Li, C. Wang, and C. Zhang, 2012: Impact of aerosols on convective clouds and precipitation. *Rev. Geophys.*, **50**, RG2001.

van den Heever, S. C., and W. R. Cotton, 2007: Urban aerosol impacts on downwind convective storms. *J. Appl. Meteor. Climatol.*, **46**, 828–850.

Wacker, U., and A. Seifert, 2001: Evolution of rain water profiles resulting from pure sedimentation: Spectral vs. parameterized description. *Atmos. Res.*, **58**, 19–39.
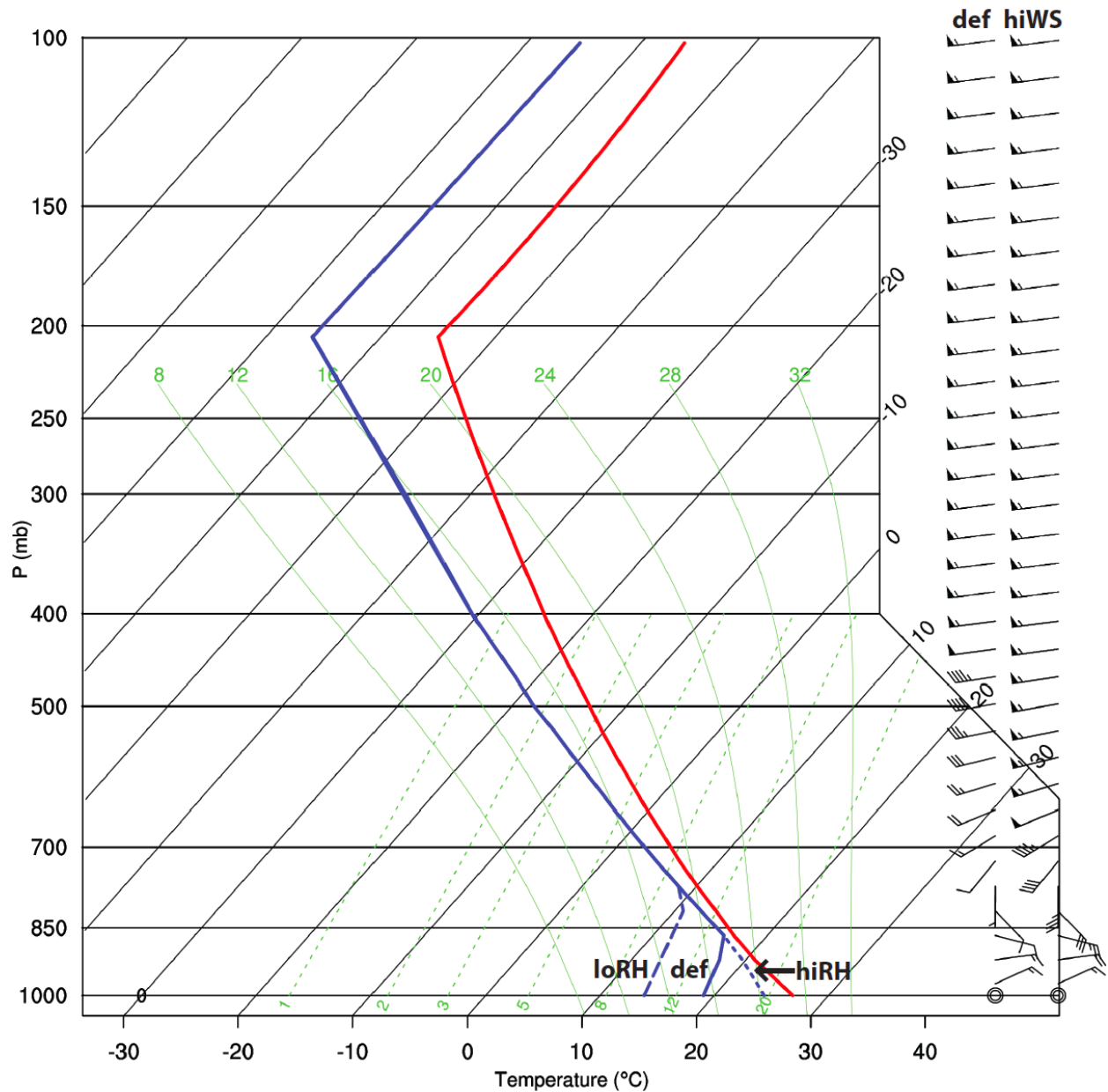
FIG. 1. Skew-T log-P diagram with the soundings used to initialize the WRF model, including the default (def) sounding and the soundings used for the sensitivity tests: low relative humidity (loRH; dashed line), high relative humidity (hiRH; dotted line), and high vertical wind shear (hiWS; rightmost wind barbs). The solid red line is the temperature profile, while the dewpoint temperature profiles are shown in blue. The wind speed and direction are represented by two sets of wind barbs on the right side of the diagram: one set for the hiWS sensitivity test and one set for all other simulations (def).
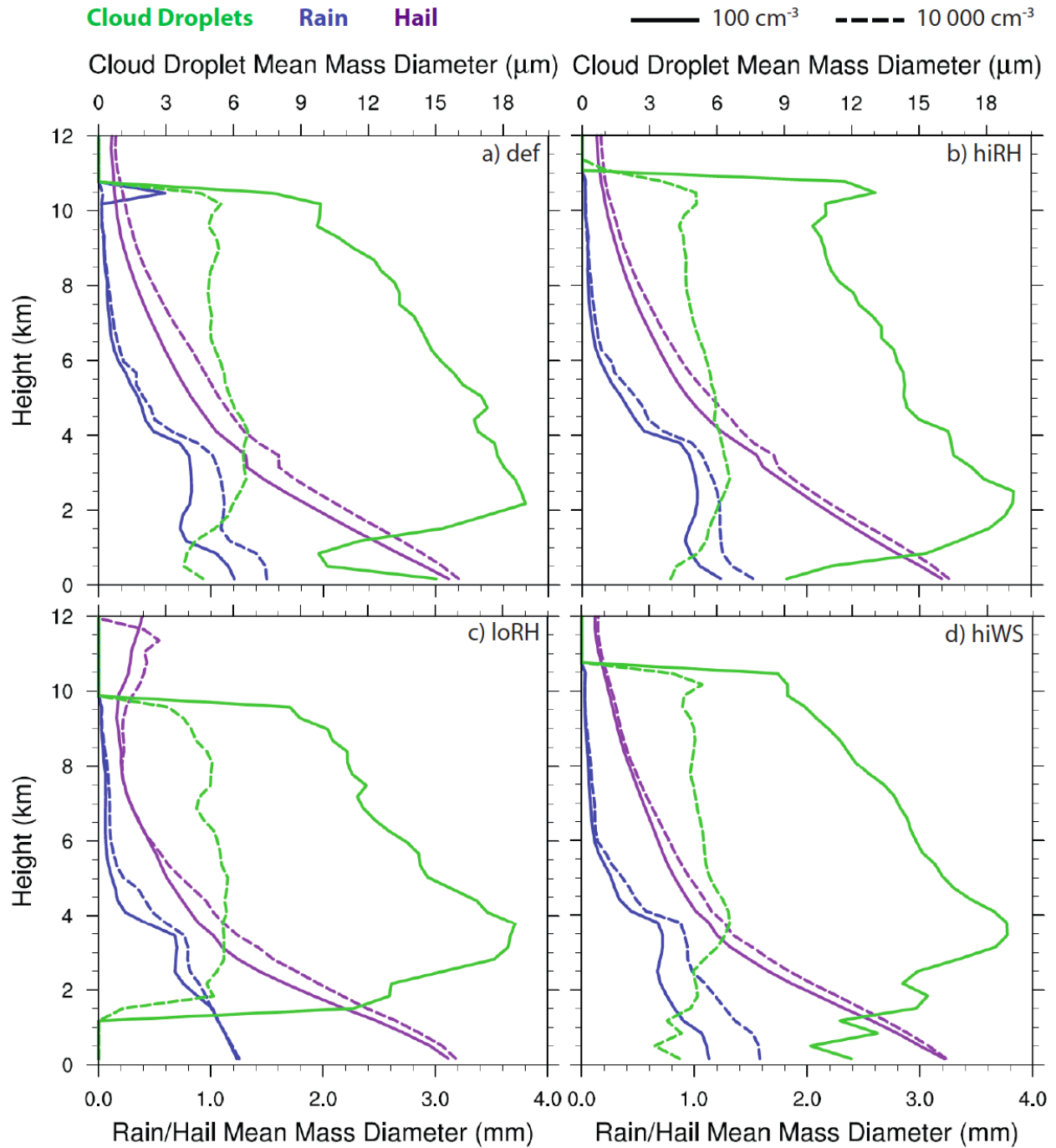
FIG. 2. Conditional, domain-averaged vertical profiles of hydrometeor mean mass diameter at t = 120 min for cloud droplets (green lines), rain (blue lines), and hail (purple lines) for a) def, b) hiRH, c) loRH, and d) hiWS soundings. Results from the cleanest (CCN = 100 cm^{-3}; solid lines) and dirtiest (CCN = 10 000 cm^{-3}; dashed lines) simulations are shown.
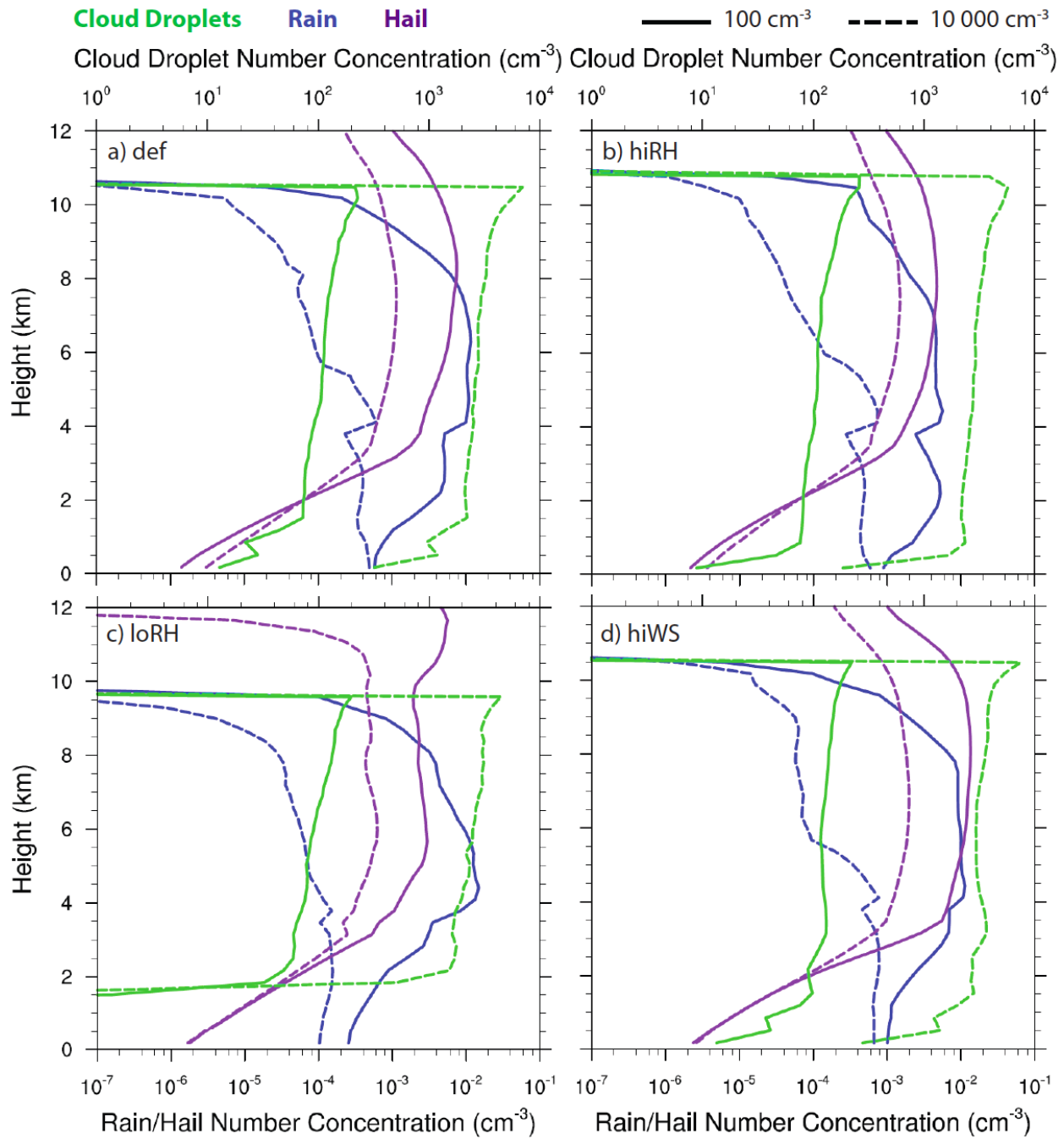
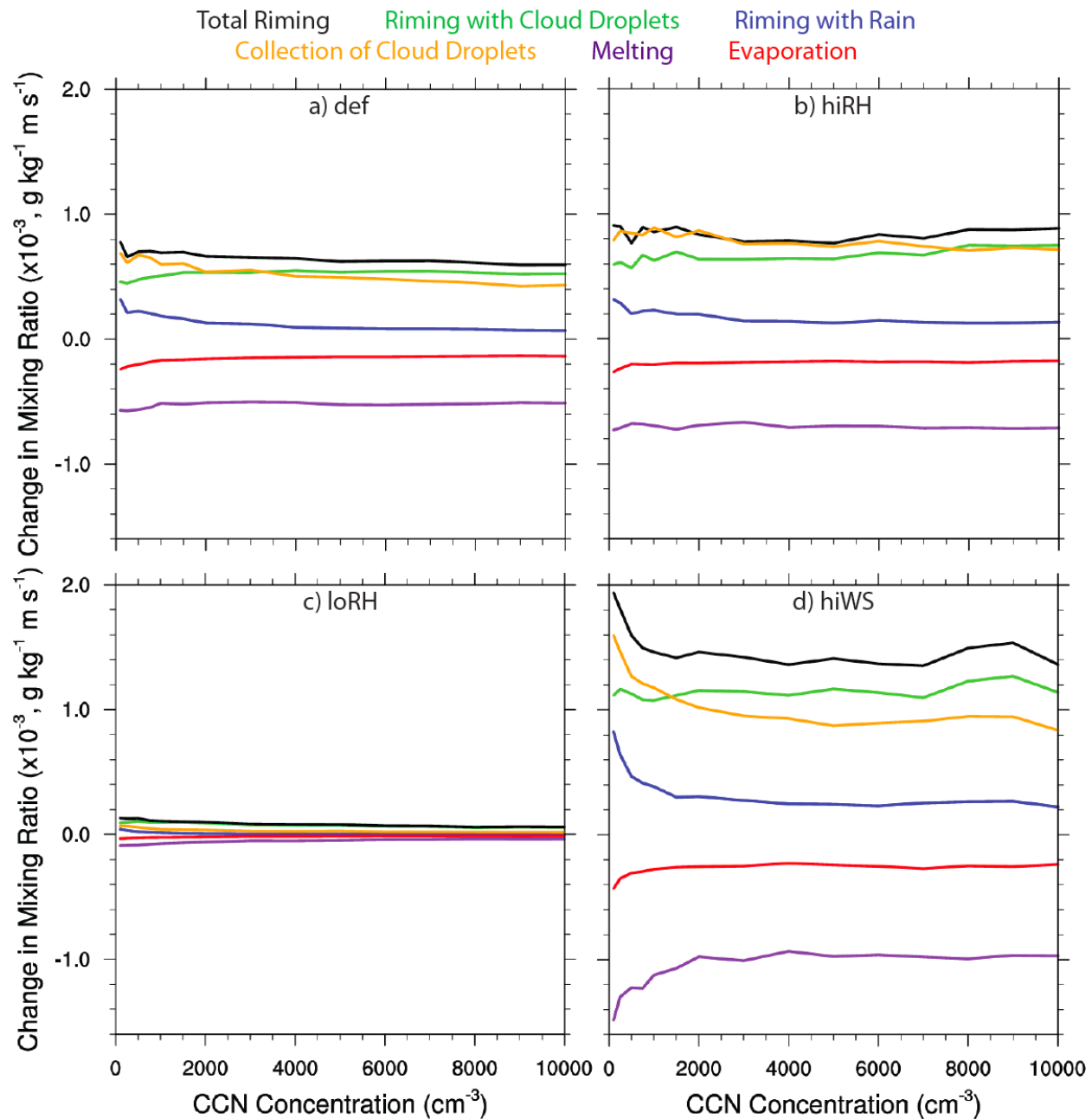FIG. 3. As in Fig. 2, but for hydrometeor number concentration.

FIG. 4. Vertically-integrated, horizontally averaged microphysical process rates versus CCN concentration at t = 120 min for a) def, b) hiRH, c) loRH, and d) hiWS soundings.
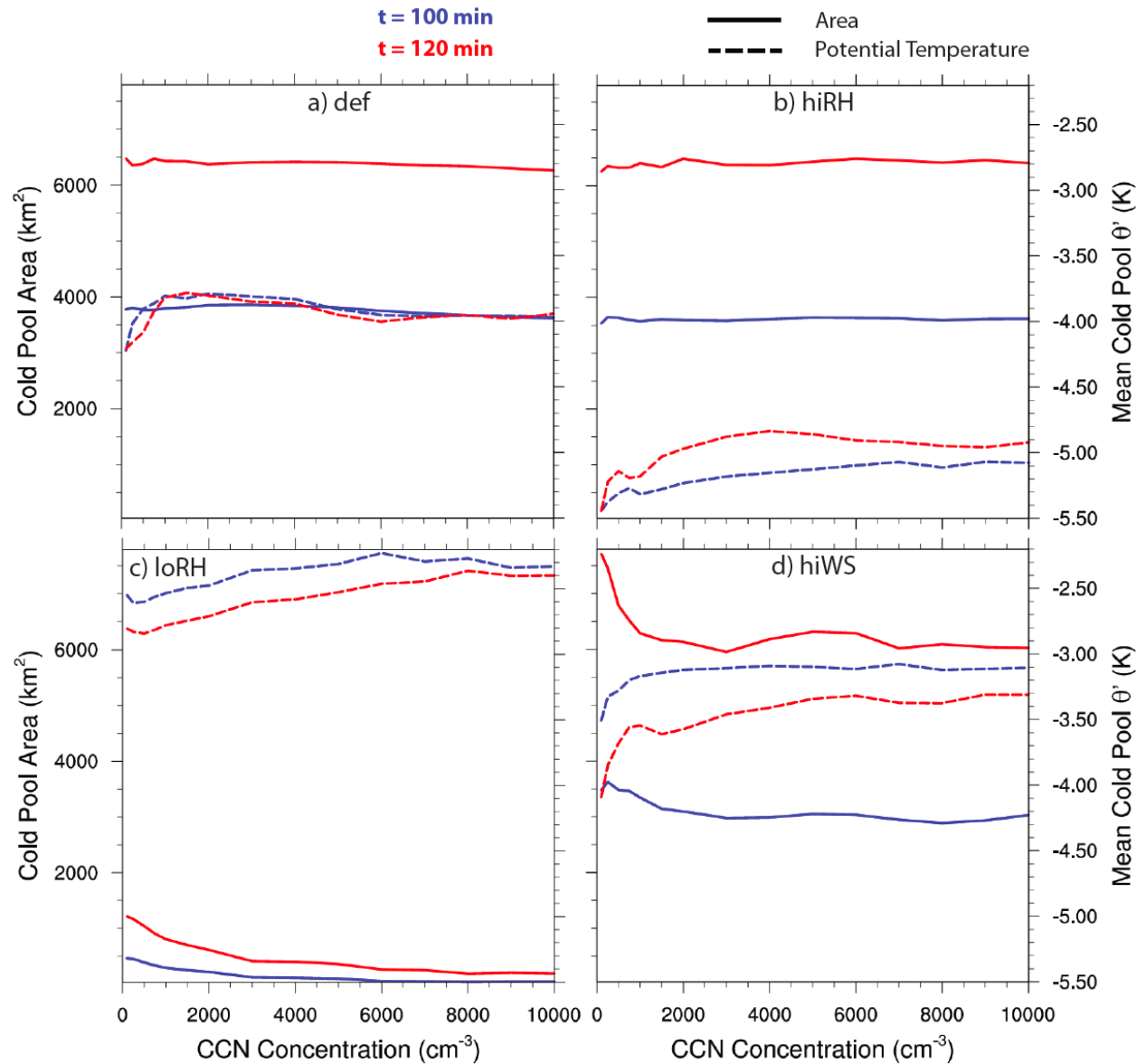
FIG. 5. Total area (solid lines) and mean perturbation potential temperature (dashed lines) of the cold pool at the lowest model level ($z = 170$ m) at $t = 100$ min (blue lines) and $t = 120$ min (red lines) versus CCN concentration for a) def, b) hiRH, c) loRH, and d) hiWS soundings.
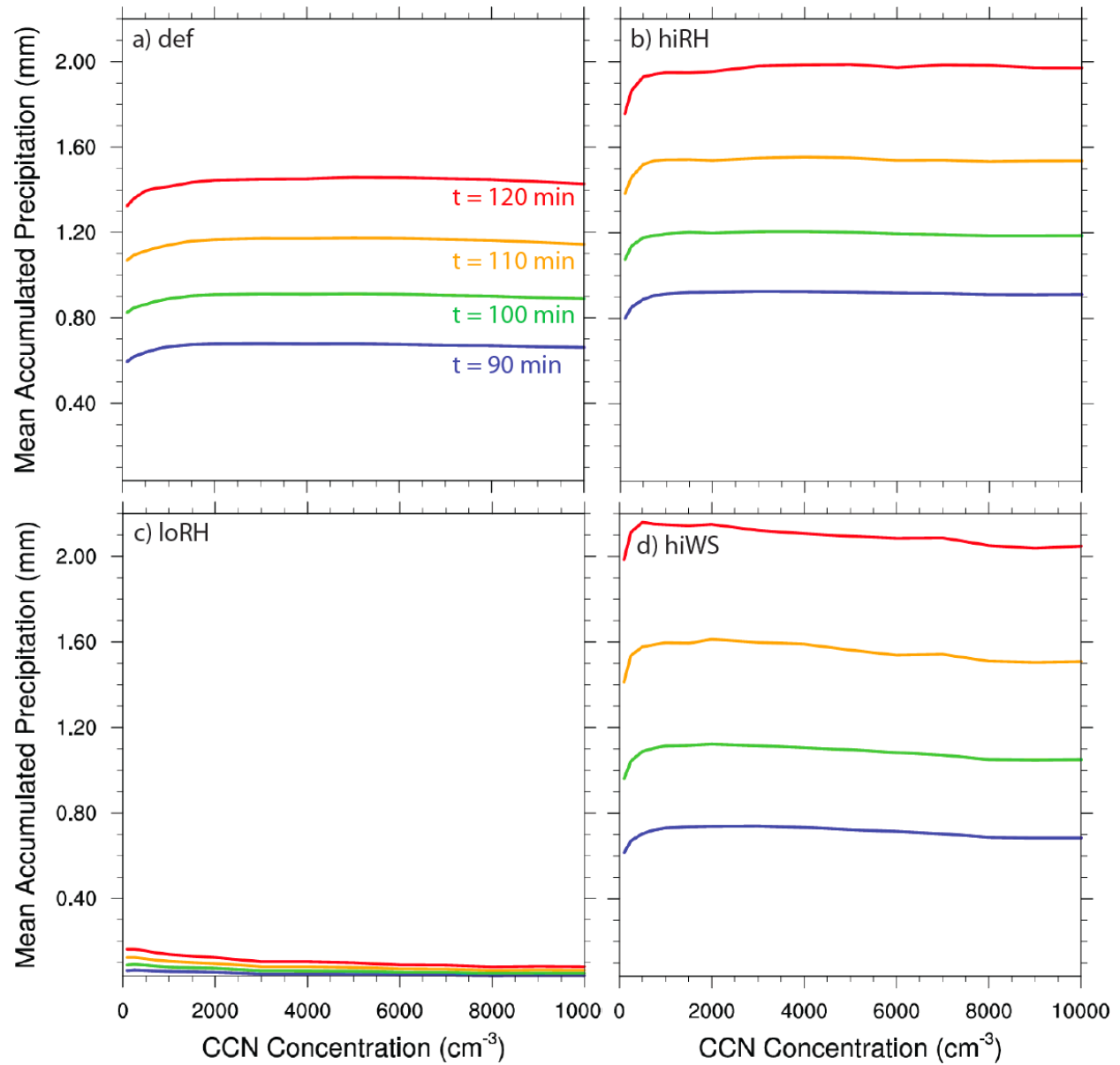
FIG. 6. Domain-averaged, accumulated surface precipitation at t = 90 min (blue line), t = 100 min (green line), t = 110 min (yellow line), and t = 120 min (red line) versus CCN concentration for a) def, b) hiRH, c) loRH, and d) hiWS soundings.
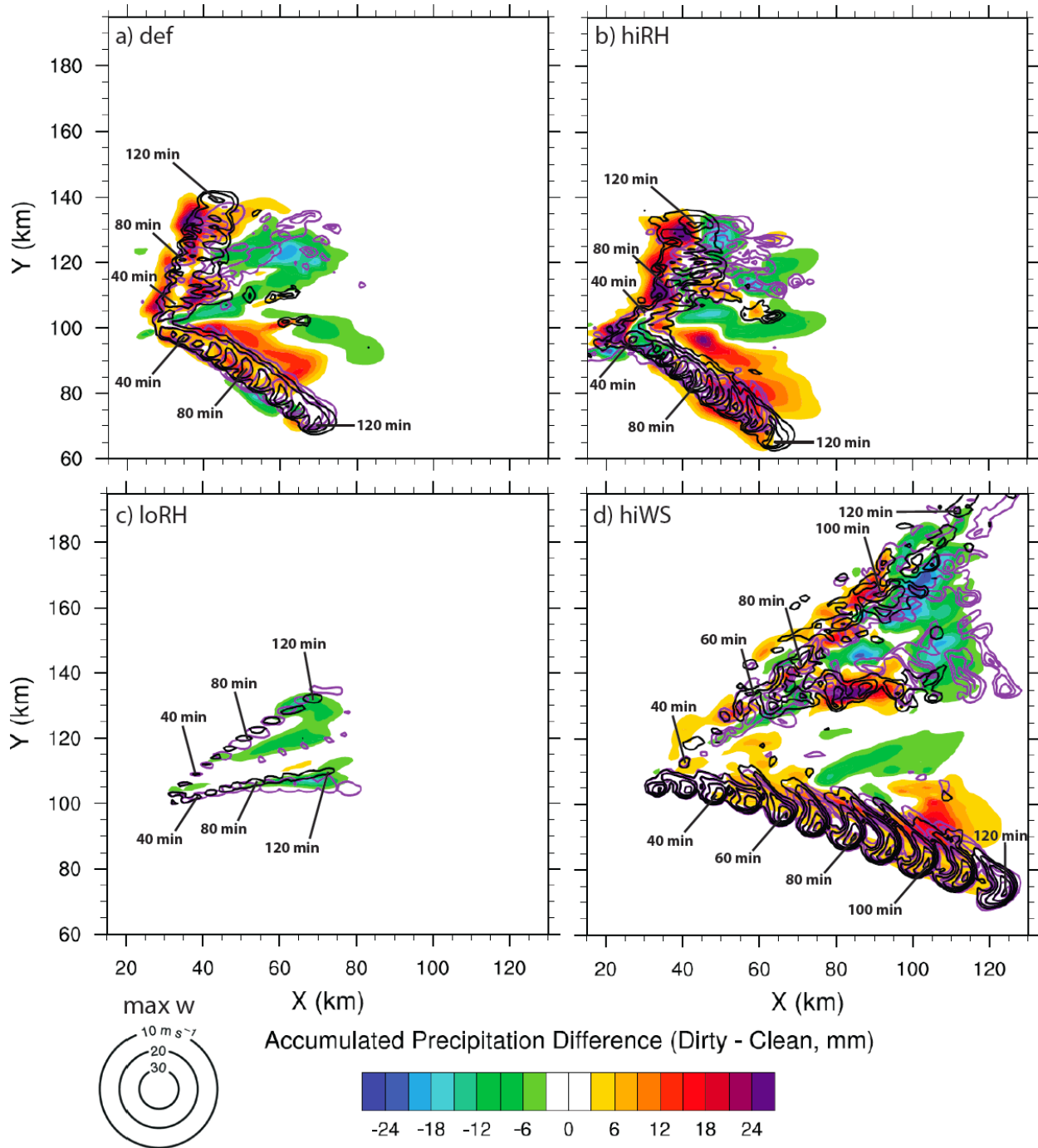
FIG. 7. Difference in accumulated surface precipitation between the dirtiest (CCN = 10 000 cm^{-3}) and cleanest (CCN = 100 cm^{-3}) simulations at t = 120 min (color fill) for a) def, b) hiRH, c) loRH, and d) hiWS soundings. The purple and black contours indicate the maximum updraft speeds that were simulated at z = 5 km for the duration of the cleanest and dirtiest simulations, respectively. These contours range from 10 m s^{-1} to 30 m s^{-1} at an interval of 10 m s^{-1}. The approximate locations of the main left- and right-moving updrafts at several times during the simulations are also indicated.